NANO LETTERS

pubs.acs.org/NanoLett Letter

Kerr Metasurface Enabled by Metallic Quantum Wells

Junxiao Zhou,[§] Haoliang Qian,[§] Ching-Fu Chen, Li Chen, and Zhaowei Liu*

Cite This: https://dx.doi.org/10.1021/acs.nanolett.0c03723 Read Online

ABSTRACT: Optical metasurfaces have emerged as promising candidates for multifunctional devices. Dynamically reconfigurable metasurfaces have been introduced by employing phase-change materials or by applying voltage, heat, or strain. While existing metasurfaces exhibit appealing properties, they do not express any significant nonlinear effects due to the negligible nonlinear responses from the typical materials used to build the metasurface. In this work, we propose and experimentally demonstrate one kind of Kerr metasurface that shows strong intensity-dependent responses. The Kerr metasurface is composed of a top layer of gold antennas, a dielectric spacer, and a ground layer of metallic quantum wells (MQWs). Because of the large Kerr nonlinearity supported by the MQWs, the effective optical properties of the MQWs can change from metallic to dielectric with increasing of the input intensity, leading to dramatic modifications of the metasurface responses. This opens up new routes for potential applications in the field of nonlinear optics.

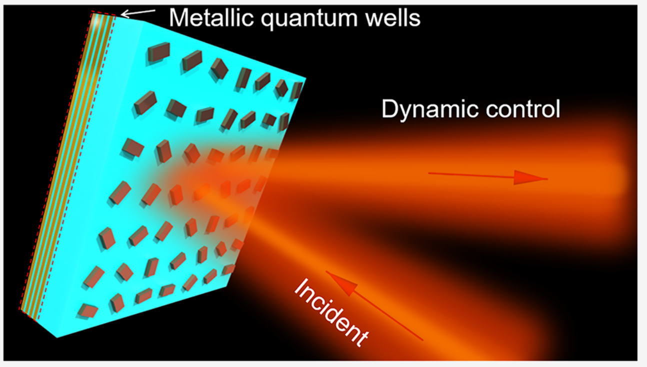

KEYWORDS: *Tunable metasurface, metallic quantum wells, beam steering, hologram*

Optical metasurfaces based on designed subwavelength metal/dielectric resonant nanostructures exhibit intriguing optical effects and applications with unprecedented properties for directing the flow of the electromagnetic radiation, which are not found by using nature material.[1−7] In particular, plasmonic metasurfaces are widely exploited for beam steering,[8] focusing,[9,10] hologram,[11−13] and so on due to their advantage of small mode volumes and high local field enhancement. Over the past decade, substantial efforts have been focused on the development of switchable, reconfigurable, and tunable plasmonic meta-devices driven by thermal,[14,15] electrostatic,[16−18] magneticstatic,[19] and stretching mechanisms.[20,21] However, the significant nonlinear-based tunability has not been achieved since all the previously used metasurface materials have very weak optical nonlinearity. Here, we first introduce and demonstrate a tunable metasurface using quantum nonlinear metamaterial composed of the metallic quantum wells (MQWs) with a large Kerr coefficient. In contrast, the technique reported here allows a large phase tuning range.

Exceptionally large Kerr nonlinearity has been recently demonstrated in 3 nm gold metallic quantum well due to its quantum size effect.[22,23] As it is known, when the thickness approaches the de Broglie wavelength, the free electrons in the metal film will be quantized into discrete energy levels,[24] where the intersubband transitions appear. Owing to the greatly enhanced dipole moment and high electron density in metals, the extreme optical nonlinearity can be engineered at desired working frequencies.[25] In fact, all plasmonic materials could be utilized to obtain strong nonlinear response based on the quantum size effect. Here, a new plasmonic material TiN comes into our view since TiN commonly is known for its CMOS compatibility, and ultrahigh thermal stability at high temperatures (melting point >2700 °C).[26,27]

Our work combines the extreme nonlinear properties in MQWs with the implementation of metasurface, as shown in Figure 1a. We introduce the quantum multilayer composed of TiN/Al_2O_3 as a tunable metamaterial, which couples with the localized plasmonic resonances of an array of gold nanoantennas forming a meta-device. When the metasurface sample is illuminated by a collimated low-intensity laser with a linear polarization, the reflected beam is being diffracted as the left- and right-handed circularly polarized (LCP and RCP) components into ±1 order, respectively. While for the case of a high-intensity laser illumination, the metasurface will act as a mirror, that is, the linear polarization remains unchanged with both RCP and LCP components reflected to its zero-order. Furthermore, a tunable hologram is demonstrated based on our proposed design. A clear image is observed when the metasurface is illuminated by a low-intensity laser, while for the high-intensity case, the image will disappear. Our finding paves

Received: September 14, 2020
Revised: December 10, 2020

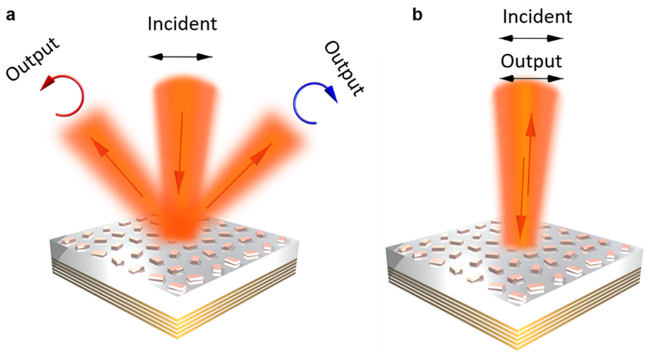

Figure 1. Schematic illustration of an intensity-dependent Kerr metasurface. (a) Linear case: under low-intensity illuminations. The red and blue arrows indicate the LCP and RCP output components, respectively. (b) Nonlinear case: under high-intensity illumination. Both input and output components are linear polarized.

the way for nonlinear optical modulators,[28] all-optical switches,[29] and reflective tunable displays.[30]

Results. *MQWs-Based Metamaterial Fabrication and Characterizations.* Figure 2 presents the characterization of the proposed TiN-Al_2O_3 MQWs-based metamaterials. Here, the TiN-Al_2O_3 superlattice is grown on a 0.5 mm-thick, c-plane oriented double-side polished sapphire substrate (see Methods, Supporting Information). The dark-field scanning transmission electron microscope (STEM) image of the cross-sectional view implies a well-formed periodic layered structure, as seen in Figure 2a. Figure 2b is a zoomed-in STEM image that shows each unit consisting of 2.4 nm TiN and 1 nm Al_2O_3. The MQWs-based metamaterials can be approximated as a uniaxial anisotropic effective medium with dielectric functions $\varepsilon_{\parallel}$ and $\varepsilon_{\perp}$ since the thickness of each layer is much smaller than the operational wavelength.[31] In this work, the optical effective permittivity of the metamaterials sample is extracted from the reflection and transmission measurement (Figure S1a,b, Supporting Information) in the low intensity case as displayed in Figure 2c. To demonstrate the tunability of our MQWs, the intensity-dependent nonlinear properties are investigated in detail. The transmission and reflection of the sample located at the beam focus are recorded at the wavelength (λ) of 800 nm as an example with the gradually increased power imposed to the sample (Figure S1c,d, Supporting Information). As shown in Figure 2d, the real part of $\varepsilon_{\parallel}$ for the MQWs increases and crosses the zero-point with the increase of incident beam intensity, while the imaginary part of $\varepsilon_{\parallel}$ shows a reverse trend, with a negative slope, decreasing with the intensity. A similar trend is seen for the $\varepsilon_{\perp}$. The huge variation of the effective permittivity is due to the large nonlinearity of the MQWs, which is further confirmed by the Z-Scan technique (Figures S2 and S3, Supporting Information).

Design of MQWs Enabled Kerr Metasurface. To confirm the nonlinear and tunable properties of the proposed MQWs-based metamaterials, a photonics spin Hall effect (PSHE) metasurface is designed. The photonic spin Hall effect recently has drawn much attention due to its potential applications in precision metrology,[32] spatial differentiation,[33] and chiroptical spectroscopy.[34] For demonstrating the large tunable range of the proposed technology, a cavity-plasmon design is employed for high optical polarization conversion efficiency (i.e., linear to circular).[6,35,36] As shown in Figure 3a, the tunable metasurface is composed of a top layer of gold nanobar, a dielectric spacer layer, and ground MQWs working as a reflecting mirror. This sandwiched design would not only obtain high converted efficiency but also guarantee the impinging transverse electric-field coupled to the desired cavity mode with both transverse and z-directions[37] (Figure S4, Supporting Information). By utilizing the geometric phase concept, opposite phase gradients could be achieved with a π-phase delay by arranging the nanobars orientation responding to the LCP and RCP beams. This leads to the circularly-polarized components reflected in opposite directions.[38,39] As shown in Figure 3b, with normal

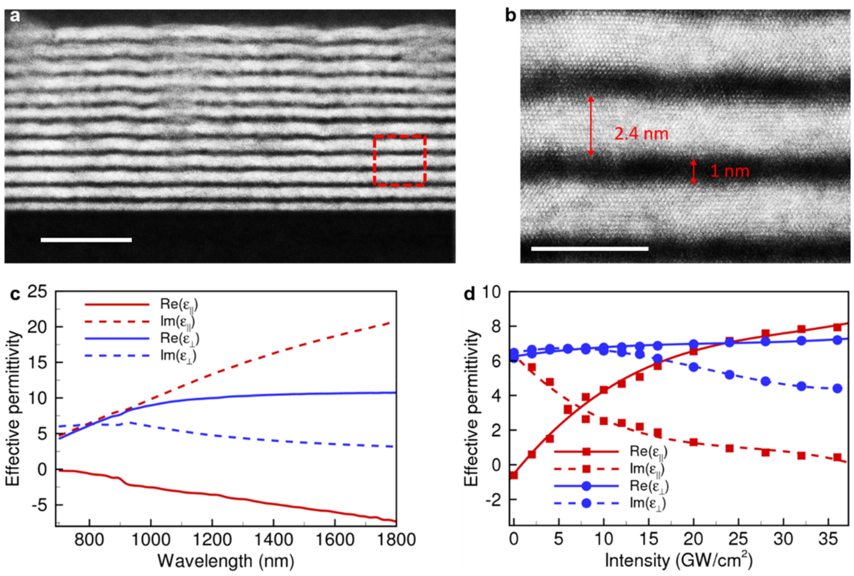

Figure 2. MQWs-based metamaterial characterization. (a) Dark-field scanning transmission electron microscope (STEM) image of the cross section of 12 pairs TiN-Al_2O_3 MQWs on sapphire substrate (thickness of each pair is 3.4 nm and the total thickness is 40.8 nm). Scale bar, 20 nm. (b) Zoomed-in STEM image (each pair consists of 2.4 nm TiN and 1 nm Al_2O_3). Scale bar, 5 nm. (c) Both the parallel and vertical permittivities of the TiN-Al_2O_3 MQWs determined from the reflection and transmission measurements. (d) Intensity-dependent permittivities (parallel and vertical) from the MQWs sample at the wavelength of 800 nm.

https://dx.doi.org/10.1021/acs.nanolett.0c03723
Nano Lett. XXXX, XXX, XXX−XXX

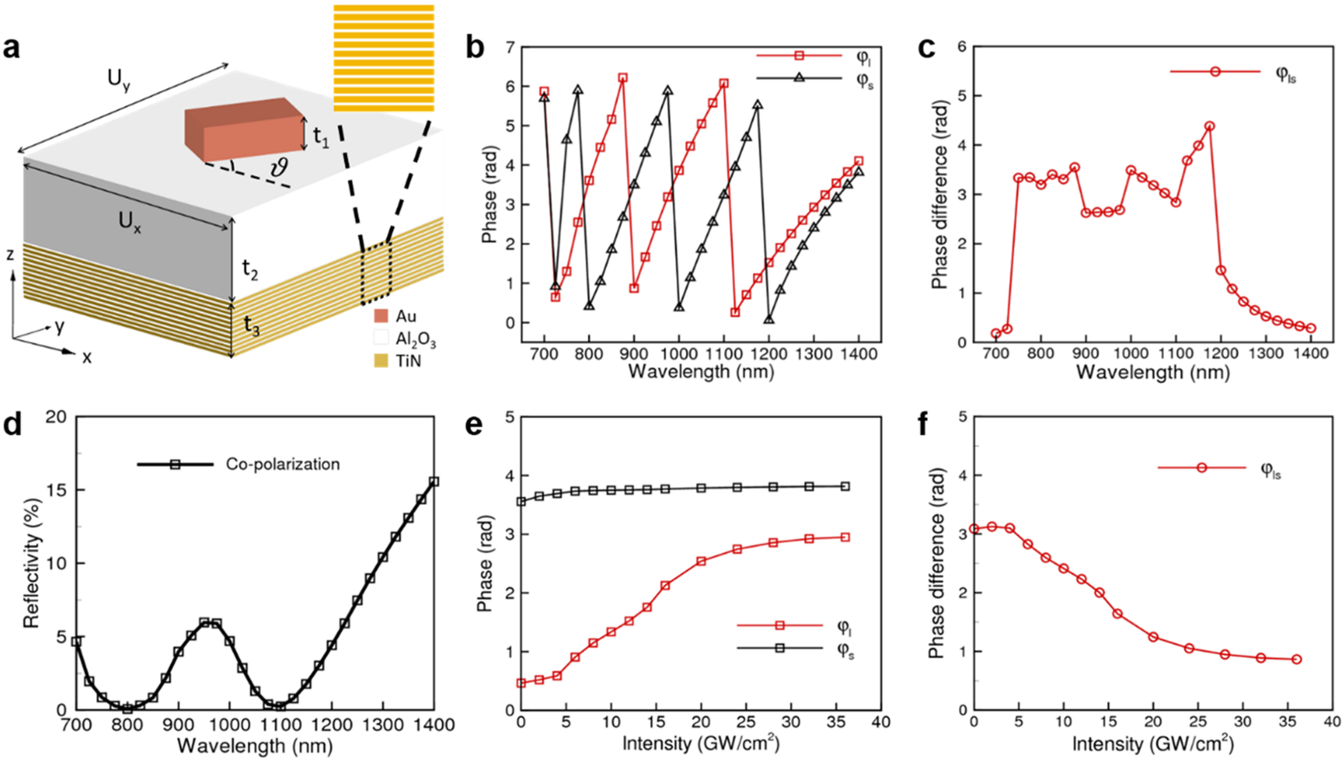

Figure 3. Design principle and its simulated of a nanobar metasurface. (a) Three-dimensional schematic view of one unit-cell consisting of gold/Al_2O_3/MQWs structure. The top nanobar is made of gold with the thickness of t_1 = 30 nm, the spacer is made of Al_2O_3 with the thickness of t_2 = 90 nm, and the bottom MQWs with the thickness of 40.8 nm. The nanobar is designed with length L = 150 nm, and width W = 60 nm, orientated in the xy plane with an angle ϑ. The unit cell is arranged with periods $U_x = U_y$ = 350 nm. (b) Simulation results of the reflection phase along long axis (φ_l) and short axis (φ_s) of the nanobar. (c) Phase difference between the long axis and short axis $\varphi_{ls} = |\varphi_l - \varphi_s|$. (d) Simulated copolarized reflectivity, which is defined as $0.25|r_x + r_y|^2$, where r_x and r_y are the complex coefficients of reflection for a single nanobar under the incident polarization along the x and y axes, respectively (Methods, Supporting Information). (e) Phase change along the long and short axes with change of input beam intensity. (f) Change of the phase difference along the long and short axes as the intensity increases.

incidence on the nanobar geometry, the simulated phase delay approaches π between the reflection coefficients of the nanobar with the incident polarizations along its long and short axes (Figure 3c) (Methods, Supporting Information).

Figure 3d shows the simulation results of the copolarized reflectivity, where the copolarized component could be extremely small by purposed design, which guarantees the high converted efficiency at the wavelength of 800 nm. The simulation result of the phase change (Figure 3e) and the phase difference (Figure 3f) with the incident polarizations along the long and short axes are demonstrated with the change of input beam intensity at the wavelength of 800 nm, where the phase modulation range of one bar could be from π to 0.28 π. Because of the geometric phase property,[38,40] the phase modulation depth of the whole metasurface is two-times one unit bar, that is, 1.44 π (2 π to 0.56 π), which ensures a large enough tunable range of our metasurface as we experimentally demonstrated. More linear and nonlinear simulation could be found in Figures S4 and S5, Supporting Information.

Experimental Demonstration of Kerr Metasurface. The proposed Kerr metasurfaces are fabricated by standard clean room processes. After TiN-Al_2O_3, MQWs are grown on the sapphire substrate, and the Al_2O_3 spacer layer is added on top by magnetron sputtering. Next, gold nanobars are patterned using the standard electron-beam lithography (Vistec EBPG5200) and lift-off processes. The top-view SEM and the cross-section view of STEM images are shown in Figure 4a and b, respectively. To characterize the spin Hall effect of the designed metasurface, a Fourier imaging setup for angular measurements is employed (Olympus IX71), as shown in Figure 4g. A Ti:Sapphire fs pulse laser (Mai-Tai oscillator Spectra Physics, 100 fs pulse duration, 80-MHz repetition rate) operating at 800 nm wavelength is used as the illumination source. A half wave plate and linear polarizer (P) are used for preparing the desired polarization state for the illumination and tuning the incident power to the sample. The followed objective with a numerical aperture of 0.45 is employed for ensuring a near-collimated beam with a diameter of 6 μm onto the metasurface and allowing the angular measurement of the reflected beams up to 27° with respect to the normal. The reflected beam modulated by the metasurface is separated by the beam splitter (BS) and imaged by lens (L) to the CCD camera. It is worth noting that the objective has the dual functionality of focusing the incident light to the desired size of the metasurface while working as a Fourier-transform-lens.

The measured reflection distributions indicate very good quantitative agreement with the simulated results of the relationship between the incident intensity and the metasurface performance. As shown in Figure 4c−f, the Fourier images correspond to four specific excitation intensities of the incident beam. The red curves on top represent the corresponding reflection intensities, with the splitting angle of LCP and RCP around 19°, which agrees well with the theoretical design as $\arcsin(\lambda/\Lambda)$. In Figure 4c, when the intensity of the incident beam is around 0.1 GW/cm^2, the reflected LCP and RCP

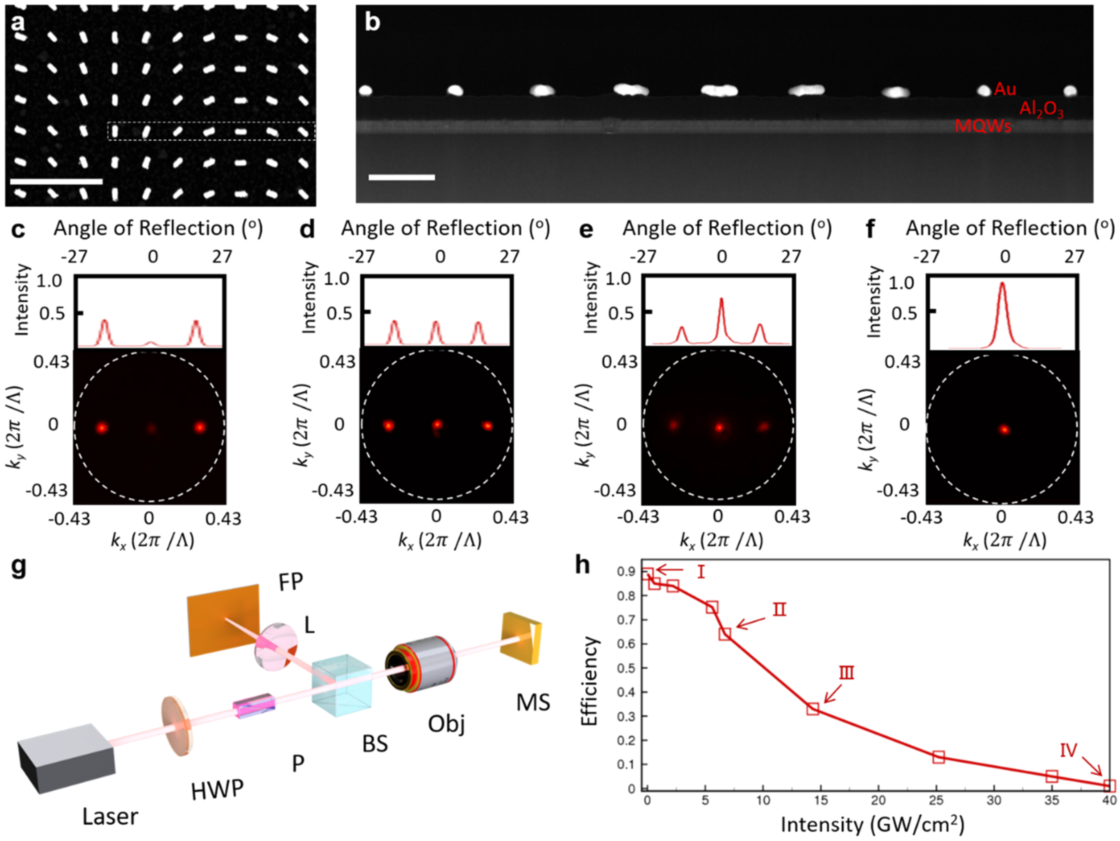

Figure 4. Experimental characterization of the tunable PSHE metasurface. (a) Top-view SEM image of the fabricated nanobar array with eight bars as one period ($\Lambda = 2.8$ μm). Scale bar, 1 μm. (b) STEM image of the cross sections for the marked white rectangle in panel a. Scale bar, 200 nm. (c−f) Experimental Fourier images of the light reflected from the metasurface at different intensities. The red curves on the top show the intensity profile along the axis of $k_y = 0$. (g) Schematic drawing of the experimental setup. HWP, half wave plate; P, polarizer; BS, beam splitter; Obj, objective; L, Lens; MS, metasurface; FP, Fourier plane. (h) Metasurface optical polarization conversion efficiency as a function of input beam intensity. The efficiency is changed as the intensity on the metasurface varied in the range from 0.1 GW/cm^2 to 40 GW/cm^2, with four corresponding intensities: (c) I intensity = 0.1 GW/cm^2, (d) II intensity = 5.6 GW/cm^2, (e) III intensity = 14.3 GW/cm^2, (f) IV intensity = 40 GW/cm^2.

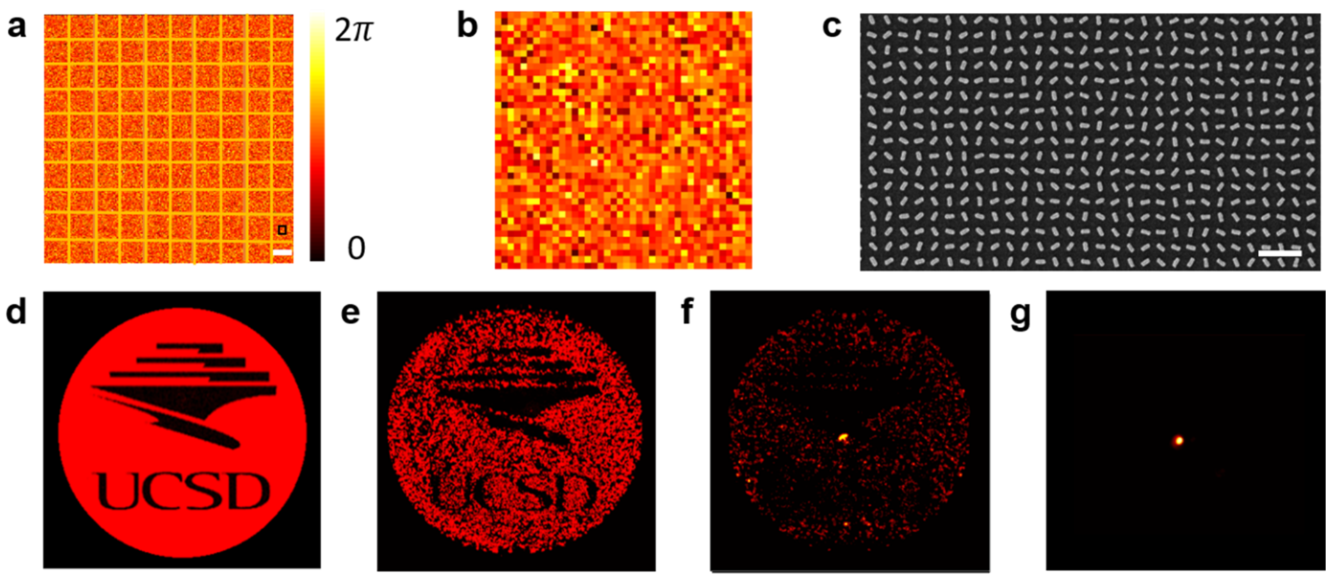

Figure 5. Sample characterization and measurement of the tunable hologram. (a) Phase distribution with 10 × 10 periods designed to generate the target holographic image in the far field. Scale bar, 90 μm. (b) Enlarged phase distribution of the lower right corner of panel a. (c) SEM image of the fabricated nanobar array (partial view). Scale bar is 1 μm. (d) Simulated holographic image of UCSD logo. (e−g) Experimentally obtained images in the far field of linear and nonlinear cases, respectively. For panels f and g, we normalized the image intensity to its highest brightness of the center spot. (d−e) Logo used with permission from UCSD.

https://dx.doi.org/10.1021/acs.nanolett.0c03723
Nano Lett. XXXX, XXX, XXX−XXX

signals contribute ~89.2% of the total reflected power. We also measured that the corresponding total reflection efficiency (the ratio between the total reflected power and the incident power) is around 40%. Therefore, the absolute efficiency attributed to the first order diffraction of the grating is around 36%. By contrast, the designed metasurface performance is tuned with the gradual increase of the incident beam intensity, and the results are presented in Figure 4d−f. Figure 4h shows the measured tunable characterization of PSHE efficiency with the intensity on the metasurface varied from 0.1 GW/cm^2 to 40 GW/cm^2. The marked symbols "I", "II", "III", and "IV" in Figure 4h correspond to the results of Figure 4c−f, respectively. It should be noted that multicycles of experiments for tunable performances are achieved, which confirms that the metasurface device is stable under the current illumination intensity (for details, see Multicycle measurements and the stability test for the metasurface section and Figures S6 and S7, Supporting Information). It is worth noting that the nonlinear response mainly comes from the MQWs instead of the top layer 30 nm Au nanobars, of which the Kerr nonlinear coefficient is three to four orders smaller than the MQWs.[22] Related simulation results could be found in the Figure S8, Supporting Information.

Kerr Metasurface Enabled Intensity-Dependent Hologram. The proposed tunable metasurface is also demonstrated for one application of intensity dependent hologram. To create the metasurface hologram, a set of the Gerchberg-Saxton algorithm is applied, which has been used for the phase-retrieve of phase-only hologram with a propagating function.[41] This computer-generated hologram has the pixel dimensions of 350 nm by 350 nm and periods of 98 μm × 98 μm with the desired phase profile of 20-phase levels (from $-\pi$ to π with an interval of $\pi/10$). To provide better holography performance, the phase profile of the hologram is merged into a 10 × 10 periodic array with a total size of 0.98 mm × 0.98 mm as shown in Figure 5a. Another advantage of using this periodic array, which is based on the concept of Dammann grating, is for avoiding the appearance of laser speckles and improving the image fidelity.[42,43] The enlarged phase distribution is displayed in Figure 5b. Figure 5c shows the SEM image of the fabricated nanobar array, of which the parameters of nanobars are the same as the previous section.

Figures 5d and e are the simulated and experimental results of the linear case when the incident power is around 0.1 GW/cm^2, respectively (experimental setup could be found in Figure S9, Supporting Information). Note that almost all energy of the incident beam is converted to desired UCSD logo image. Here, the illuminated pattern area of our metasurface is very small to reach enough incident intensity to fulfill the nonlinear requirement, which leads to the low image quality. When the intensity of the incident beam is increased to 20 GW/cm^2, the intensity ratio between the UCSD logo and the zero order is decreased, as shown in Figure 5f. With the intensity increased to 30 GW/cm^2 (Figure 5g), the whole UCSD logo image disappears, which further demonstrates the high nonlinear properties and large-range tunable mechanism. Our full-range tunable nonlinear control opens the door to existing photonic applications in the visible and infrared regime.

Discussion and Conclusion. The demonstrated tunable phenomena could be regarded as an ultrafast optical switch. For example, based on the results of Figure 4, when the input intensity is smaller than 1 GW/cm^2, the reflection remains constant. This may be considered as the ON mode of the proposed all-optical switch. When the input intensity reaches higher values than I_{in} = 40 GW/cm^2, the metasurface will lose its performance, going to OFF mode. Again, when the intensity drops below I_{in} = 1 GW/cm^2, the metasurface goes back to ON operation.

In summary, we have proposed a tunable metasurface consisting of a top layer of gold nanobars, a dielectric spacer layer, and ground MQWs-based metamaterials. As a demonstration, the tunable spin Hall effect is achieved to confirm the proposed technique. Moreover, the tunable hologram is demonstrated to further confirm the performance of tunable metasurface. In principle, our tunability design and application are not limited to a single wavelength but with a broadband working range covering from the visible to the near-infrared. In additional, the phase modulation depth could be around 100%. The demonstration of the proposed technique may find potential application in ultrafast nonlinear optical switch and tunable display.

■ ASSOCIATED CONTENT

Supporting Information

The Supporting Information is available free of charge at https://pubs.acs.org/doi/10.1021/acs.nanolett.0c03723.

Growth of TiN/Al_2O_3 metallic quantum wells; simulation details; RT measurement for effective permittivity extraction; Z-scan measurement for the nonlinear property; wavelength dependent nonlinearity; experimental setup of tunable hologram (PDF)

■ AUTHOR INFORMATION

Corresponding Author

Zhaowei Liu − *Department of Electrical and Computer Engineering and Materials Science and Engineering, University of California, San Diego, La Jolla, California 92093, United States;* orcid.org/0000-0002-5732-8109; Email: zhaowei@ucsd.edu

Authors

Junxiao Zhou − *Department of Electrical and Computer Engineering, University of California, San Diego, La Jolla, California 92093, United States;* orcid.org/0000-0001-6168-8580

Haoliang Qian − *Department of Electrical and Computer Engineering, University of California, San Diego, La Jolla, California 92093, United States*

Ching-Fu Chen − *Department of Electrical and Computer Engineering, University of California, San Diego, La Jolla, California 92093, United States*

Li Chen − *Materials Science and Engineering, University of California, San Diego, La Jolla, California 92093, United States*

Complete contact information is available at: https://pubs.acs.org/10.1021/acs.nanolett.0c03723

Author Contributions

[§]J.Z. and H.Q. contributed equally to this work. Z.L. initiated the project. J.Z. and H.Q. designed the materials and devices. H.Q. and C.-F.C. performed the sample growth. J.Z. and H.Q. performed the sample characterization and experiments. J.Z. and L.C. performed the numerical simulation. H.Q. performed the quantum well theoretical calculation. J.Z. and H.Q. did the measurement. All authors analyzed the data and wrote the manuscript. Z.L. supervised the research.

Notes

The authors declare no competing financial interest.

ACKNOWLEDGMENTS

The authors would like to thank Qian Ma and Junxiang Zhao for contributing to valuable discussions. This work is supported by the Defense Advanced Research Projects Agency (DARPA) DSO-NLM Program (Grant No. HR00111820038).

REFERENCES

(1) Yu, N.; Genevet, P.; Kats, M. A.; Aieta, F.; Tetienne, J.-P.; Capasso, F.; Gaburro, Z. Light Propagation with Phase Discontinuities: Generalized Laws of Reflection and Refraction. *Science* **2011**, *334*, 333−337.

(2) Ni, X.; Emani, N. K.; Kildishev, A. V.; Boltasseva, A.; Shalaev, V. M. Broadband Light Bending with Plasmonic Nanoantennas. *Science* **2012**, *335*, 427−427.

(3) Lin, D.; Fan, P.; Hasman, E.; Brongersma, M. L. Dielectric Gradient Metasurface Optical Elements. *Science* **2014**, *345*, 298−302.

(4) Ginn, J. C.; Brener, I.; Peters, D. W.; Wendt, J. R.; Stevens, J. O.; Hines, P. F.; Basilio, L. I.; Warne, L. K.; Ihlefeld, J. F.; Clem, P. G.; et al. Realizing Optical Magnetism from Dielectric Metamaterials. *Phys. Rev. Lett.* **2012**, *108*, No. 097402.

(5) Moitra, P.; Yang, Y.; Anderson, Z.; Kravchenko, I. I.; Briggs, D. P.; Valentine, J. Realization of an All-Dielectric Zero-Index Optical Metamaterial. *Nat. Photonics* **2013**, *7*, 791.

(6) Sun, S.; Yang, K.-Y.; Wang, C.-M.; Juan, T.-K.; Chen, W. T.; Liao, C. Y.; He, Q.; Xiao, S.; Kung, W.-T.; Guo, G.-Y.; et al. High-Efficiency Broadband Anomalous Reflection by Gradient Meta-Surfaces. *Nano Lett.* **2012**, *12*, 6223−6229.

(7) Wang, S.; Wu, P. C.; Su, V.-C.; Lai, Y.-C.; Chu, C. H.; Chen, J.-W.; Lu, S.-H.; Chen, J.; Xu, B.; Kuan, C.-H.; Li, T.; Zhu, S.; Tsai, D. P. Broadband Achromatic Optical Metasurface Devices. *Nat. Commun.* **2017**, *8*, 187.

(8) Kildishev, A. V.; Boltasseva, A.; Shalaev, V. M. Planar Photonics with Metasurfaces. *Science* **2013**, *339*, 1232009.

(9) Chen, X.; Huang, L.; Mühlenbernd, H.; Li, G.; Bai, B.; Tan, Q.; Jin, G.; Qiu, C.-W.; Zhang, S.; Zentgraf, T. Dual-Polarity Plasmonic Metalens for Visible Light. *Nat. Commun.* **2012**, *3*, 1198.

(10) Wang, S.; Wu, P. C.; Su, V.-C.; Lai, Y.-C.; Chen, M.-K.; Kuo, H. Y.; Chen, B. H.; Chen, Y. H.; Huang, T.-T.; Wang, J.-H.; Lin, R.-M.; Kuan, C.-H.; Li, T.; Wang, Z.; Zhu, S.; Tsai, D. P. A Broadband Achromatic Metalens in the Visible. *Nat. Nanotechnol.* **2018**, *13*, 227.

(11) Wen, D.; Yue, F.; Li, G.; Zheng, G.; Chan, K.; Chen, S.; Chen, M.; Li, K. F.; Wong, P. W. H.; Cheah, K. W.; et al. Helicity Multiplexed Broadband Metasurface Holograms. *Nat. Commun.* **2015**, *6*, 8241.

(12) Zheng, G.; Mühlenbernd, H.; Kenney, M.; Li, G.; Zentgraf, T.; Zhang, S. Metasurface Holograms Reaching 80% Efficiency. *Nat. Nanotechnol.* **2015**, *10*, 308.

(13) Sun, S.; Zhou, Z.; Zhang, C.; Yang, W.; Song, Q.; Xiao, S. All-Dielectric Meta-Reflectarray for Efficient Control of Visible Light. *Ann. Phys.* **2018**, *530*, 1700418.

(14) Ou, J.-Y.; Plum, E.; Jiang, L.; Zheludev, N. I. Reconfigurable Photonic Metamaterials. *Nano Lett.* **2011**, *11*, 2142−2144.

(15) Tao, H.; Strikwerda, A.; Fan, K.; Padilla, W.; Zhang, X.; Averitt, R. Reconfigurable Terahertz Metamaterials. *Phys. Rev. Lett.* **2009**, *103*, 147401.

(16) Ou, J.-Y.; Plum, E.; Zhang, J.; Zheludev, N. I. An Electromechanically Reconfigurable Plasmonic Metamaterial Operating in the near-Infrared. *Nat. Nanotechnol.* **2013**, *8*, 252−255.

(17) Holsteen, A. L.; Cihan, A. F.; Brongersma, M. L. Temporal Color Mixing and Dynamic Beam Shaping with Silicon Metasurfaces. *Science* **2019**, *365*, 257−260.

(18) Huang, Y.-W.; Lee, H. W. H.; Sokhoyan, R.; Pala, R. A.; Thyagarajan, K.; Han, S.; Tsai, D. P.; Atwater, H. A. Gate-Tunable Conducting Oxide Metasurfaces. *Nano Lett.* **2016**, *16*, 5319−5325.

(19) Lapine, M.; Shadrivov, I. V.; Powell, D. A.; Kivshar, Y. S. Magnetoelastic Metamaterials. *Nat. Mater.* **2012**, *11*, 30.

(20) Pryce, I. M.; Aydin, K.; Kelaita, Y. A.; Briggs, R. M.; Atwater, H. A. Highly Strained Compliant Optical Metamaterials with Large Frequency Tunability. *Nano Lett.* **2010**, *10*, 4222−4227.

(21) Ee, H.-S.; Agarwal, R. Tunable Metasurface and Flat Optical Zoom Lens on a Stretchable Substrate. *Nano Lett.* **2016**, *16*, 2818−2823.

(22) Qian, H.; Xiao, Y.; Liu, Z. Giant Kerr Response of Ultrathin Gold Films from Quantum Size Effect. *Nat. Commun.* **2016**, *7*, 13153.

(23) Xiao, Y.; Qian, H.; Liu, Z. Nonlinear Metasurface Based on Giant Optical Kerr Response of Gold Quantum Wells. *ACS Photonics* **2018**, *5*, 1654−1659.

(24) Arora, V. K.; Awad, F. G. Quantum Size Effect in Semiconductor Transport. *Phys. Rev. B: Condens. Matter Mater. Phys.* **1981**, *23*, 5570.

(25) Qian, H.; Li, S.; Chen, C.-F.; Hsu, S.-W.; Bopp, S. E.; Ma, Q.; Tao, A. R.; Liu, Z. Large Optical Nonlinearity Enabled by Coupled Metallic Quantum Wells. *Light: Sci. Appl.* **2019**, *8*, 13.

(26) Naik, G. V.; Schroeder, J. L.; Ni, X.; Kildishev, A. V.; Sands, T. D.; Boltasseva, A. Titanium Nitride as a Plasmonic Material for Visible and near-Infrared Wavelengths. *Opt. Mater. Express* **2012**, *2*, 478−489.

(27) Guler, U.; Boltasseva, A.; Shalaev, V. M. Refractory Plasmonics. *Science* **2014**, *344*, 263−264.

(28) Xu, B.; Martinez, A.; Yamashita, S. Mechanically Exfoliated Graphene for Four-Wave-Mixing-Based Wavelength Conversion. *IEEE Photonics Technol. Lett.* **2012**, *24*, 1792−1794.

(29) Van, V.; Ibrahim, T.; Ritter, K.; Absil, P.; Johnson, F.; Grover, R.; Goldhar, J.; Ho, P.-T. All-Optical Nonlinear Switching in Gaas-Algaas Microring Resonators. *IEEE Photonics Technol. Lett.* **2002**, *14*, 74−76.

(30) Duan, X.; Kamin, S.; Liu, N. Dynamic Plasmonic Colour Display. *Nat. Commun.* **2017**, *8*, 14606.

(31) Elser, J.; Podolskiy, V. A.; Salakhutdinov, I.; Avrutsky, I. Nonlocal Effects in Effective-Medium Response of Nanolayered Metamaterials. *Appl. Phys. Lett.* **2007**, *90*, 191109.

(32) Zhou, X.; Ling, X.; Luo, H.; Wen, S. Identifying Graphene Layers Via Spin Hall Effect of Light. *Appl. Phys. Lett.* **2012**, *101*, 251602.

(33) Zhou, J.; Qian, H.; Chen, C.-F.; Zhao, J.; Li, G.; Wu, Q.; Luo, H.; Wen, S.; Liu, Z. Optical Edge Detection Based on High-Efficiency Dielectric Metasurface. *Proc. Natl. Acad. Sci. U. S. A.* **2019**, *116*, 11137−11140.

(34) Shaltout, A.; Liu, J.; Kildishev, A.; Shalaev, V. Photonic Spin Hall Effect in Gap−Plasmon Metasurfaces for on-Chip Chiroptical Spectroscopy. *Optica* **2015**, *2*, 860−863.

(35) Pors, A.; Albrektsen, O.; Radko, I. P.; Bozhevolnyi, S. I. Gap Plasmon-Based Metasurfaces for Total Control of Reflected Light. *Sci. Rep.* **2013**, *3*, 2155.

(36) Pors, A.; Nielsen, M. G.; Eriksen, R. L.; Bozhevolnyi, S. I. Broadband Focusing Flat Mirrors Based on Plasmonic Gradient Metasurfaces. *Nano Lett.* **2013**, *13*, 829−834.

(37) Todorov, Y.; Andrews, A. M.; Colombelli, R.; De Liberato, S.; Ciuti, C.; Klang, P.; Strasser, G.; Sirtori, C. Ultrastrong Light-Matter Coupling Regime with Polariton Dots. *Phys. Rev. Lett.* **2010**, *105*, 196402.

(38) Bomzon, Z. e.; Biener, G.; Kleiner, V.; Hasman, E. Space-Variant Pancharatnam−Berry Phase Optical Elements with Computer-Generated Subwavelength Gratings. *Opt. Lett.* **2002**, *27*, 1141−1143.

(39) Hasman, E.; Kleiner, V.; Biener, G.; Niv, A. Polarization Dependent Focusing Lens by Use of Quantized Pancharatnam−Berry Phase Diffractive Optics. *Appl. Phys. Lett.* **2003**, *82*, 328−330.

https://dx.doi.org/10.1021/acs.nanolett.0c03723
Nano Lett. XXXX, XXX, XXX−XXX

(40) Bomzon, Z. e.; Kleiner, V.; Hasman, E. Pancharatnam−Berry Phase in Space-Variant Polarization-State Manipulations with Subwavelength Gratings. *Opt. Lett.* **2001**, *26*, 1424−1426.
(41) Gerchberg, R. W. A Practical Algorithm for the Determination of Phase from Image and Diffraction Plane Pictures. *Optik* **1972**, *35*, 237−246.
(42) Dammann, H.; Görtler, K. High-Efficiency in-Line Multiple Imaging by Means of Multiple Phase Holograms. *Opt. Commun.* **1971**, *3*, 312−315.
(43) Feldman, M. R.; Guest, C. C. Iterative Encoding of High-Efficiency Holograms for Generation of Spot Arrays. *Opt. Lett.* **1989**, *14*, 479−481.

https://dx.doi.org/10.1021/acs.nanolett.0c03723
Nano Lett. XXXX, XXX, XXX−XXX